AIAA paper 2015-3932, 2015, 51st AIAA/SAE/ASEE Joint Propulsion Conference, 27-30 July 2015, Orlando, FL

Simulation of Stall Inception of a High Speed Axial Compressor with Rotor-Stator Interaction

Jiaye Gan *
Hong-Sik Im †
Ge-Cheng Zha‡
Dept. of Mechanical and Aerospace Engineering, University of Miami
Coral Gables, Florida 33124, USA

August 7, 2015

Abstract

This paper solves unsteady Reynolds-averaged Navier-Stokes (URANS) equations to simulate stall inception of NASA compressor stage 35 with rotor-stator interaction. A full annulus of the rotor-stator stage is simulated with an interpolation sliding boundary condition (BC) to resolve the rotor-stator interaction. The tip clearance is fully gridded to accurately resolve tip vortices and its effect on stall inception. The unsteady simulation indicates that the inception of rotating stall in Stage 35 is spike inception. The stall cells grow quickly and brings the rotor to full stall within roughly 1.2 revolutions. The stall cell propagates at about 90% of rotor speed in the counter rotor rotation direction in relative the frame.

1 Introduction

Rotating stall usually starts from tip span. The roles of tip clearance vortex, passage shock and their interactions on stall inception are important to understand. Tip clearance vortex breakdown is considered as one of the causes for stall inception of some rotors[1]. For high-speed compressors, the pattern of flow breakdown during the stall or surge is not well understood due to the effects of compressibility, difficulties in detailed measurement, shaft speed, and geometry. Hah et al.[2] numerically studied stall inception in a forward-swept transonic compressor rotor. There is no tip clearance vortex breakdown during the operation of rotor, even in the stall condition. The passage shock oscillation is considered as one of the courses that drive the stall inception. Recently, Reuss et al.[3] tested a jet engine high pressure compressor to investigate the effect of inlet total pressure distortions on rotating stall. Their experiment shows that the spike type stall cell moves at approximately 60% of the compressor speed. After two to three more revolutions, rotating stall is established. The speed of the rotating stall cell is reduced to about 45% of the compressor speed and its length scale is roughly 50% of the annulus.

The stall inception of NASA stage 35 is done numerically by several research groups. Mina et al.[4] carried out numerical simulation of rotating stall inception for NASA stage 35 using a single passage. It is observed that at near stall, the tip vortex grows larger in size and its trajectory becomes perpendicular to the main axial flow. A low-momentum area near rotor tip leading edge causes the flow spillage and leads to stall inception. Davis and Yao[5] also used NASA stage 35 single blade passage to investigate stall inception. Their finding agrees with Hoying et al.[6] who shows that the circulation of tip clearance vortex plays an important role in stall inception development. Vo[7] conducted rotating stall simulation for a low speed rotor with relative tip Mach number of 0.2 and the transonic NASA stage 35 rotor using six blade

*AIAA Member, Ph.D. student
†AIAA Member, Ph.D., Currently a senior engineer at Honeywell
‡Professor, gzha@miami.edu

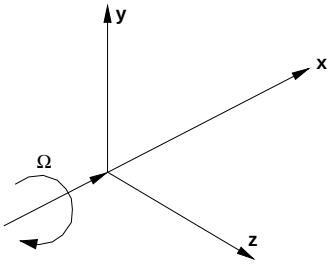

Figure 1: The Cartesian system rotating with angular velocity Ω around the x-axis

passages. Their results show that leading edge tip clearance flow has spillage below blade tip and back flow at the trailing-edge at the onset of spike. Chen et al.[8, 9] conducted a full annulus simulation of NASA Stage 35 at the full speed using an unsteady RANS(URANS) model. In their simulation, a simplified "roof top" type tip clearance mesh is used to model the tip clearance flow. Their results show that a disturbance first travels at the rotor speed, then changes to a spike disturbance of 84% rotor speed consisting of multiple stall cells. The disturbance eventually forms a single rotating stall cell of 43% rotor speed[8]. Most of the aforementioned Stage 35 stall inception simulation employs the "roof top" tip griding.

The purpose of this paper is to investigate the stall inception of Stage 35 with full griding of the tip clearance to accurately simulate the stall inception. The stall inception of Stage 35 captured in this study does not appear to be the modal inception as obtained by Chen et al[8, 9], but a spike inception. It is not clear at this time whether the difference is from the tip clearance treatment or other numerical modeling such as turbulence model etc.

2 Numerical Methods

The unsteady Reynolds-averaged Navier-Stokes (URANS) equations are solved in a rotating frame[10] with the Spalart-Allmaras (SA) turbulence model[11]. A shock capturing scheme is necessary to simulate high-speed axial compressors since most rotor blades experience shock/boundary layer interaction. In this study the Low Diffusion E-CUSP (LDE) Scheme[12] as an accurate shock capturing Riemann solver is used with a 3rd order WENO reconstruction for inviscid flux and a 2nd order central differencing for viscous terms[13]. An implicit 2nd order dual time stepping method[14] using unfactored Gauss-Seidel line iteration is utilized to achieve high convergence rate. The high-scalability parallel computing is implemented to save wall clock time[15].

2.1 Governing Equations

The equation of motion of fluid flow for turbomachinery in a rotating frame of reference as shown in Fig. 1 can be derived in order to take into account the Coriolis force ($2\Omega\times\mathbf{V}$) and the centrifugal force($\Omega\times\Omega\times\mathbf{r}$). Applying coordinate transformation to the generalized coordinate system(ξ,η,ζ), the dimensionless Reynolds averaged 3D Navier-Stokes equations coupled with the SA model can be expressed as the following conservative form:

$$\frac{\partial \mathbf{Q}}{\partial t}+\frac{\partial \mathbf{E}}{\partial \xi}+\frac{\partial \mathbf{F}}{\partial \eta}+\frac{\partial \mathbf{G}}{\partial \zeta}=\frac{1}{Re}\left(\frac{\partial \mathbf{E}_v}{\partial \xi}+\frac{\partial \mathbf{F}_v}{\partial \eta}+\frac{\partial \mathbf{G}_v}{\partial \zeta}+\mathbf{S}\right) \tag{1}$$

where Re is the Reynolds number. The equations are nondimenisonalized based on airfoil chord L_∞, freestream density ρ_∞, velocity U_∞, and viscosity μ_∞. The conservative variable vector $\mathbf{Q}$, the inviscid flux vector $\mathbf{E}$, the viscous flux vector $\mathbf{E_v}$ and the source term vector $\mathbf{S}$ are expressed as follows and the rest can be expressed following the symmetric rule.

$$\mathbf{Q} = \frac{1}{J}\begin{pmatrix} \bar{\rho} \\ \bar{\rho}\tilde{u} \\ \bar{\rho}\tilde{v} \\ \bar{\rho}\tilde{w} \\ \bar{\rho}\tilde{e} \\ \rho\tilde{\nu} \end{pmatrix} \tag{2}$$

$$\mathbf{E} = \begin{pmatrix} \bar{\rho}U \\ \bar{\rho}\tilde{u}U + l_x\bar{p} \\ \bar{\rho}\tilde{v}U + l_y\bar{p} \\ \bar{\rho}\tilde{w}U + l_z\bar{p} \\ \left(\bar{\rho}\tilde{e} + \bar{p}\right)U - l_t\bar{p} \\ \rho\tilde{\nu}U \end{pmatrix} \tag{3}$$

$$\mathbf{E_v} = \begin{pmatrix} 0 \\ l_k\bar{\tau}_{xk} \\ l_k\bar{\tau}_{yk} \\ l_k\bar{\tau}_{zk} \\ l_k\left(\tilde{u}_i\bar{\tau}_{ki} - \bar{q}_k\right) \\ \frac{\bar{\rho}}{\sigma}\left(\nu + \tilde{\nu}\right)\left(\mathbf{l} \bullet \nabla\tilde{\nu}\right) \end{pmatrix} \tag{4}$$

$$\mathbf{S} = \frac{1}{J}\begin{pmatrix} 0 \\ 0 \\ \bar{\rho}R_eR_o{}^2y + 2\bar{\rho}R_eR_ow \\ \bar{\rho}R_eR_o{}^2z - 2\bar{\rho}R_eR_ov \\ 0 \\ S_v \end{pmatrix} \tag{5}$$

$$\begin{gathered} S_v = \rho c_{b1}\left(1 - f_{t2}\right)\tilde{S}\tilde{\nu} \\ +\tfrac{1}{Re}\left[-\rho\left(c_{w1}f_w - \tfrac{c_{b1}}{\kappa^2}f_{t2}\right)\left(\tfrac{\tilde{\nu}}{d}\right)^2\right. \\ \left.+\tfrac{\rho}{\sigma}c_{b2}\left(\nabla\tilde{\nu}\right)^2 - \tfrac{1}{\sigma}\left(\nu + \tilde{\nu}\right)\nabla\tilde{\nu} \bullet \nabla\rho\right] \\ +Re\left[\rho f_{t1}\left(\Delta q\right)^2\right] \end{gathered} \tag{6}$$

where R_o is the Rossby number defined as $\frac{\Omega L_\infty}{U_\infty}$. ρ is the density, p is the static pressure, and e is the total energy per unit mass. The overbar denotes Reynolds averaged variable, and the tilde is used to denote the Favre averaged variable. ν is kinematic viscosity and $\tilde{\nu}$ is the working variable related to eddy viscosity in SA model. U, V and W are the contravariant velocities in ξ, η, ζ directions. For example, U is defined as follows.

$$U = l_t + \mathbf{l} \bullet \mathbf{V} = l_t + l_x\tilde{u} + l_y\tilde{v} + l_z\tilde{w} \tag{7}$$

$$l_t = \frac{\xi_t}{J}d\eta d\zeta, \qquad \mathbf{l} = \frac{\nabla\xi}{J}d\eta d\zeta \tag{8}$$

When the grid is stationary, $l_t = 0$. In the current discretization, $\Delta\xi = \Delta\eta = \Delta\zeta = 1$.

Let the subscripts i, j, k represent the coordinates x, y, z and use the Einstein summation convention. By introducing the concept of eddy viscosity to close the system of equations, the shear stress $\bar{\tau}_{ik}$ and total heat flux $\bar{q}_k$ in Cartesian coordinates can be expressed in tensor form as

$$\bar{\tau}_{ik} = \left(\mu + \mu_t\right)\left[\left(\frac{\partial\tilde{u}_i}{\partial x_k} + \frac{\partial\tilde{u}_k}{\partial x_i}\right) - \frac{2}{3}\delta_{ik}\frac{\partial\tilde{u}_j}{\partial x_j}\right] \tag{9}$$

$$\bar{q}_k = -\left(\frac{\mu}{Pr} + \frac{\mu_t}{Pr_t}\right)\frac{\partial \tilde{T}}{\partial x_k} \tag{10}$$

Above Eq.(9) and (10) are transformed to the generalized coordinate system in computation. The molecular viscosity μ is determined by Sutherland's law, and μ_t is determined by the SA model[16].

$$\mu_t = \bar{\rho}\tilde{\nu} f_{v1} \tag{11}$$

where

$$f_{v1} = \frac{\chi^3}{\chi^3 + c_{v1}^3}, \quad \chi = \frac{\tilde{\nu}}{\nu}$$
$$r = \frac{\tilde{\nu}}{R_e \tilde{S} k^2 d^2}, \quad \tilde{S} = S + \frac{\tilde{\nu}}{R_e k^2 d^2} f_{v2}, \quad f_{v2} = 1 - \frac{\chi}{1+\chi f_{v1}}$$
$$S = \sqrt{2\omega_{ij}\omega_{ij}}, \quad \omega_{ij} = \frac{1}{2}\left(\frac{\partial u_i}{\partial x_j} - \frac{\partial u_j}{\partial x_i}\right)$$

The rest of auxiliary relations and the values of the coefficients given by reference[16] are used. The equation of state as a constitutive equation relating density to pressure and temperature is given as follows;

$$\bar{\rho}\tilde{e} = \frac{\bar{p}}{(\gamma - 1)} + \frac{1}{2}\bar{\rho}(\tilde{u}^2 + \tilde{v}^2 + \tilde{w}^2) - \frac{1}{2}\bar{\rho} r^2 R_o^2 \tag{12}$$

where $r(= \sqrt{y^2 + z^2})$ is the normalized radius from the rotating axis, x. For simplicity, all the bar and tilde in above equations will be dropped in the rest of this paper.

2.2 Implicit Time Integration

The time dependent governing equation (1) is solved using dual time stepping method suggested by Jameson[17]. A pseudo temporal term $\frac{\partial Q}{\partial \tau}$ is added to the governing Eq. (1). This term vanishes at the end of each physical time step and has no influence on the accuracy of the solution. An implicit pseudo time marching scheme using Gauss-Seidel line relaxation is employed to achieve high convergence rate instead of using an explicit scheme[14]. The pseudo temporal term is discretized with first order Euler scheme. Let m stand for the iteration index within a physical time step, the semi-discretized governing equation can be expressed as

$$\begin{aligned}\left[\left(\frac{1}{\Delta\tau} + \frac{1.5}{\Delta t}\right) I - \left(\frac{\partial R}{\partial \mathbf{Q}}\right)^{n+1,m}\right] \delta\mathbf{Q}^{\mathbf{n+1,m+1}} \\ = R^{n+1,m} - \frac{3\mathbf{Q}^{\mathbf{n+1,m}} - 4\mathbf{Q}^{\mathbf{n}} + \mathbf{Q}^{\mathbf{n-1}}}{2\Delta t}\end{aligned} \tag{13}$$

where $\Delta\tau$ is the pseudo time step, n is the physical time step index, and R is the net flux of the discretized Navier-Stokes equations evaluated at a grid point.

2.3 Interpolation Rotor/Stator Sliding BC

For unsteady rotor-stator interaction simulation, the rotor mesh will rotate with the rotor blades and the stator mesh will be stationary. Solving the Navier-Stokes equations requires transferring the fluxes between these two meshes. In [18], a conservative sliding BC is developed by making the meshes on both side of the sliding boundary one-to-one connected. Even though the conservative BC is mathematically more rigorous, it is not convenient to make a multi-block mesh one-to-one connected. For engineering applications, independent mesh for rotor and stator is desirable for efficient setup of a simulation. This paper thus adopts an interpolation sliding BC with high accuracy to remove the requirement that the rotor and stator mesh needs to be one-to-one connected.

The working mechanism of present interpolation rotor/stator sliding BC is sketched in Fig. 2, where S1, S2, S3, S4 and R1, R2, R3 are the arbitrary computational mesh cells of the stator and rotor in the circumferential direction on the two sides of the sliding interface. The current interpolation sliding boundary condition is based on the same radial distribution of the mesh on both side of the sliding boundary.

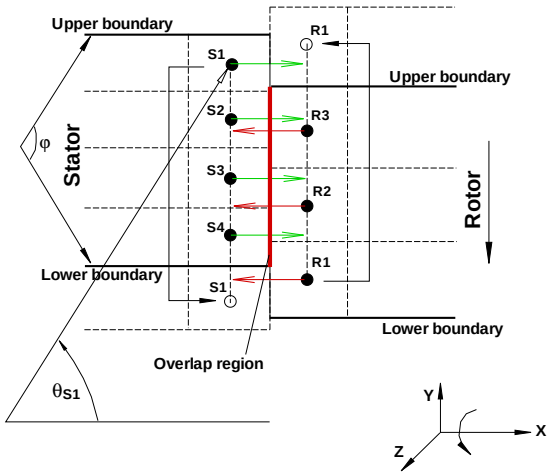

Figure 2: Working mechanism of interpolation rotor/stator sliding BC

To interpolate the conservative variable vector $\mathbf{Q}$, the circumferential mesh angle is first obtained at each mesh cell center, e.g. the angle of a stator cell s1, θ_{s1} can be defined as $tan^{-1}(z/y)_{s1}$. Then, two adjacent mesh angles in the opposite interface corresponding to current mesh cell are found for linear interpolation, e.g. $\mathbf{Q}$ at R3 is interpolated in terms of $(\theta_{R3} - \theta_{S2})$ and $(\theta_{S3} - \theta_{S2})$ as given in Eq. (14). Note that a rotation rule based on the geometric periodicity is used to interpolate $\mathbf{Q}$ in the non-overlap region, e.g. $\mathbf{Q_{S1}}$ is rotated by the periodic sector angle (φ) to interpolate $\mathbf{Q_{R1}}$ vice versa for $\mathbf{Q_{R1}}$.

$$\mathbf{Q}_{R3} = \frac{\theta_{R3} - \theta_{s2}}{\theta_{s3} - \theta_{s2}}(\mathbf{Q}_{s3} - \mathbf{Q}_{s2}) + \mathbf{Q}_{s2} \tag{14}$$

Since the frame of reference taken in this study is a fixed frame for the stationary blades and a moving relative frame for the rotor, the following exchange relations between the fixed and moving relative frame are used.

$$\begin{pmatrix} \rho \\ \rho u \\ \rho v_r \\ \rho(v_\theta + rR_o) \\ \rho(e + c_\theta r R_o) \end{pmatrix}_{Fixed} \rightleftharpoons \begin{pmatrix} \rho \\ \rho u \\ \rho v_r \\ \rho v_\theta \\ \rho e \end{pmatrix}_{Moving} \tag{15}$$

2.4 Other Boundary Conditions

At the inlet, the radial distributions of total pressure, total temperature, swirl angle and pitch angle are specified and the velocity is extrapolated from the computational domain in order to determine the rest of the variables. On the blade surface a non-slip boundary condition is applied, while an efficient wall function BC[10] is used on the hub/casing surface where y^+ is greater than 11 to avoid an excessive fine mesh in the endwall boundary layer. At the stator outlet, the static pressure is specified in the spanwise direction. The velocity components are extrapolated from the computational domain and an isentropic relation is used to determine density. The hub/casing wall static pressure for the inviscid momentum equation is determined by solving the radial equilibrium equation, whereas the static pressure gradient across the wall boundary is set to zero for the blade wall surface. An adiabatic condition is used to impose zero heat flux through the wall.

3 Results and discussion

The transonic axial compressor, NASA stage 35 that consists of 36 rotor blades and 46 stator blades[19], is simulated to investigate the stall inception mechanism using the interpolation rotor/stator sliding BC. The total pressure ratio of NASA stage 35 at design speed of 17189 rpm is 1.82. Full annulus of stage 35 with geometry periodic sector simulated and the mesh is shown in Fig.3. An O-mesh topology around blades and H-mesh for stage inlet/outlet duct region are used. The rotor tip clearance is modeled using a fully grided O-mesh. In the tip gap, 11 grid points are placed radially. Total mesh points of the full annulus are about 16 million with 482 blocks. The physical time step size is determined to allow about 40 unsteady steps per rotor blade passing.

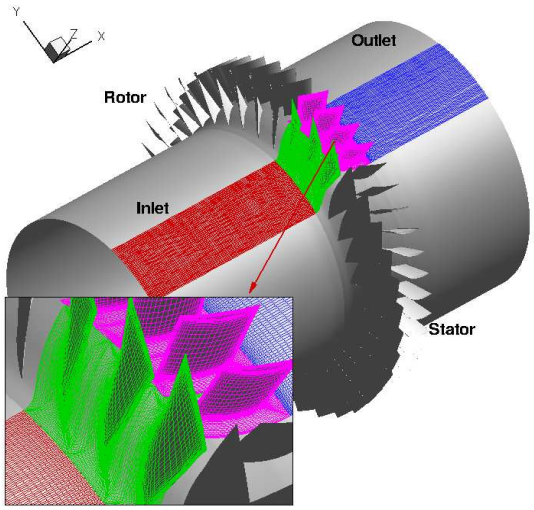

Figure 3: Full annulus mesh of NASA stage 35

Fig.4 shows the predicted speedline for NASA Stage 35 using steady state single blade passage with mixing plane boundary condition on the rotor and stator interface. A refined mesh of total 550,750 grid points and a coarse mesh (main mesh) of 449,790 grid points per blade passage are used for the mesh refinement study using the mixing plane[18]. The speedline predicted by the two meshes shows good agreement. Therefore, the coarse mesh is used to construct the full annulus mesh in Fig.3. The simulation is conducted at 4004 test condition[19] since the measured radial profiles for CFD comparison are available. The mass flows at choke condition predicted by both unsteady rotor/stator interaction and steady mixing plane are about 20.82 kg/s, which is about 0.62% lower than the measured choke flow of 20.95 kg/s[19].

The circumferential mass averaged total pressure ratio, total temperature ratio, adiabatic efficiency and absolute flow angle at stage outlet are compared with the measurement at 4004 point[19] in Fig.5. Overall good agreement with the experiment is achieved by both approaches; the mixing plane and the interpolation rotor/stator sliding BC.

Fig.6 shows instantaneous entropy at mid span of the compressor. The wake propagates well through the rotor/stator interface smoothly. Fig.7 compares the instantaneous normalized mass flux ρU (top) and static pressure P (bottom) right upstream and downstream of the interface, which indicates excellent flux conservation through the rotor/stator interface. Fig.6 and Fig.7 use the half annulus to validate the interpolating sliding BC. The simulation of stall inception in the following section employs full annulus.

3.1 Stall Pressure Rise Characteristics

The predicted unsteady stage speedline is illustrated in Fig.8, which starts from the near stall point P2. It can be seen that pressure drop is after the near stall point is nearly linear. Fig.9 shows the variations of mass flow rate during rotating stall. Although the pressure rise start to drop at P2 as shown in Fig.8,

it can be see that the mass flow drops slowly up to 1.0T (T is the rotating time in one rotor revolution) and decrease rapidly after that. The primary stalling phenomenon at P4 is that rotating stall quickly grows toward inner span with the occurrence of the second stall cell, which will be further discussed in the following sections.

3.2 Rotating Stall Onset and Propagation

The static pressure time history can be used to investigate the stall characteristics. Fig.10 shows the circumferential distributions of the normalized static pressure located at 50% tip chord length upstream of rotor at different time. Note that the curves of pressure are moved with an offset of 2 at different time. At t=14.0T(P3), the flow aound the full annulus is periodic and no disturbances are observed. The variation of static pressure through full annuls appear to have sharp shape, which indicates there exit strong shocks near the leading edge of the rotor. At t=14.5T(near P4), the flow is disturbed from part of the annulus, where the annulus region containing the disturbance is from $310^\circ \sim 10^\circ$, which shows that the stall cell size at this moment cover about 5 to 6 passages. The non-uniform pressure indicate the onset of the spike type rotating stall. After about 1.1T(P9), the flow around the entire full annulus is disturbed and lose its periodicity. The propagation speed of the stall cell can be roughly calculated from this plot and equal to 90.0% of the rotor speed. At t= 15.75T and t= 16.0T, the variation of pressure become random. Note that the sharp edge shapes of pressure distribution disapper after t=15.5T and are lost due to shock waves move to more upstream.

The circumferential distributions of the upstream axial velocity(U_x) at the rotor tip span are shown in Fig.11. The time history of U_x is similar to that of pressure. At the beginning, the axial velocity periodic variation caused by blade passing and passage shock is dominant, as shown at P3. The spike type disturbance appear at P4 with the disturbed axial velocity. The non-periodicity continues to grow to full annulus until P9.

Rotating stall is usually initiated from rotor tip. To capture the rotating stall, the numerical probes are hence located about 50% tip chord length upstream and downstream at the rotor tip span. The term 'stall cell' used in the current study is to describe a continuous structure of disturbances. Fig.12 shows the variations of instantaneous static pressure and axial velocity at the rotor tip upstream. At about 14.5T, a spike like disturbance travling with full rotor speed is seen. The stall cell speed can be determined by the angle of pressure/velocity field rotation and the duration. The spike disburbance continues to rotate and and transport to more blade passage with about 90% rotor speed. After 1.5T, the stall cells propagate at 50% of the rotor speed in the opposite direction of the rotor rotation. The rotating stall is fully developed within 1.2 rotor revolutions. Chen et al.[8] recently reported the stall inception of NASA Stage 35 with numerical simulation. In their observations, modal disturbance is found before 2 rotor revolutions and then transform into spike disturbance. The variations of axial velocity follow the same behavior as that of pressure, but the propagating speed of the stall cell is more clear. And we can roughly calculate the propagating speed of the stall cell from this plot.

Fig.13 illustrates entropy contours in axial cross section near rotor leading edge. Entropy stands for the degree of energy loss, and high entropy reflects the stalled portion of the annulus. At 14.57T(near stall onset), one continuous high entropy regions can be seen. The primary stall cell is identified by about 5 stalled passages. It is shown that the stall cell starts from the rotor tip area, and grows along the circumference as well as inward. Fig.13 also indicates that the upper 70% of blade span is stalled within 1.2T.

Fig.14 shows instantaneous negative axial velocity contour at 4 different time near the rotor tip span. The negative axial velocity represents the stalled area. The reverse flow can be seen in all rotor passages due to the tip clearance vortex flow. The pattern of reverse flow is almost the same in every passage at t=14.44T. The distribution of negative axial velocity becomes different at t=14.56T, which indicates the onset of stall. And the upstream regular flow structure near the leading edge of the blades is breakdown by the stall cell at t=14.78T.

The instantaneous variations of static pressure at the mid tip clearance span are shown in Fig.15. It

is seen from this figure that the flow near the leading edge of some blade passages is disturbed due to the interaction of shock wave and tip clearance vortex at t=14.44T, which indicates the stall inception of the compressor. As the rotor rotating, the stall cell propagates in the opposite direction of rotor revolution and grows rapidly. The flow blockage region becomes bigger and bigger and the unsymmetrical pressure distribution around the circumference can be detected. At t=15.0T, the non-uniform flow near the tip span covers most of the rotor passages. Furthermore, it is evident that the rotating stall diffuses very rapidly downstream of rotor and interacts with stator, which creates a significant amount of unsteadiness.

Fig.16 shows the relative Mach number contours across the 6 rotor blade passages where the stall inception occurs. At t=14.11T, the detached shock waves are uniform and close to the leading edge of rotor blade. The shock wave and tip vortex interaction phenomena at suction side can be observed. The shock wave fronts are pushed further upstream by the flow blockage and become non-uniform at t=14.56T. After t=15.0T, it can be seen that the shock wave fronts are almost disappear in upstream region of rotor. And low momentum flow covers most of leading edge near the tip span. It is note that the stall cell at the original location grows slowly in the direction of casing to hub as most of shock wave dominated flow structures are uniform since the 75% span, which indicates the propagating speed of stall cell in circuferencial direction is much faster than the speed in inward direction. This can also be seen in Fig.13.

The vortex cores and surrounded streamlines identified in the rotor passage are illustrated in Fig.17. At t=14.11T away from the stall inception, the trajectory of the tip vortex is oblique and may interact with pressure side of adjacent blades. At t=14.56T near stall inception, the trajectory of the vortex core is align perpendicularly to the axial direction which indicates the spikes like stall inception as discussed Hoying[6]. However, the tip vortex breakdown phenomena are not clearly seen during the stall onset. The tip vortex breakdown occurrence is used as a criteria for the cause of stall inception by many people[20, 21, 22, 23, 1]. In present study, there is no breakdown to the tip clearance vortex occurred during the onset of the stall. The breakdown of the tip clearance vortex happen after t=14.78T.

4 Conclusions

The URANS was conducted to investigate rotating stall inception mechanism in a full annulus transonic rotor NASA Stage 35 with sliding interpolation BC. The predicted stage performance have a good agreement with the experiment. The details of the flow breakdown that lead to fully developed rotating stall are well captured by the present numerical methods.

The simulation shows that the rotor stall onset is spike like disturbance with inlet total pressure perturbation. The stall disturbance at the rotor tip span propagation starts at the speed of at 100% of the rotor speed in the opposite direction of rotor rotation. The size of the onset stall cell cover about 5 to 6 rotor blade passage. The stall inception occurs at roughly 14.5T. The stall cell grows to the whole annulus roughly within 1.2 rotor revolutions after the stall inception. The propagation speed of stall cell is about 90% of rotor rotating speed.

The tip clearance vortex breakdown was not observed in present study during the the onset of stall. The interaction between shock wave and tip leakage vortex appears to be the cause of stall. The trajectory of tip clearance vortex is perpendicular to the leading edge when the rotor begins to stall.

Acknowledgment

The grant support from AFRL and the industrial partners of GUIde Consortium, 10-AFRL-1024 and 09-GUIDE-1010, are acknowledged.

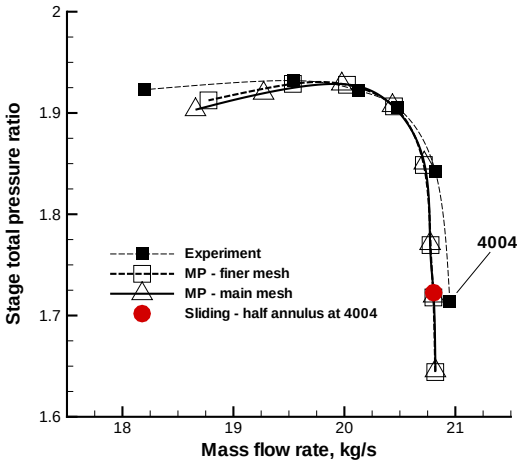

Figure 4: Predicted speedline of NASA stage 35

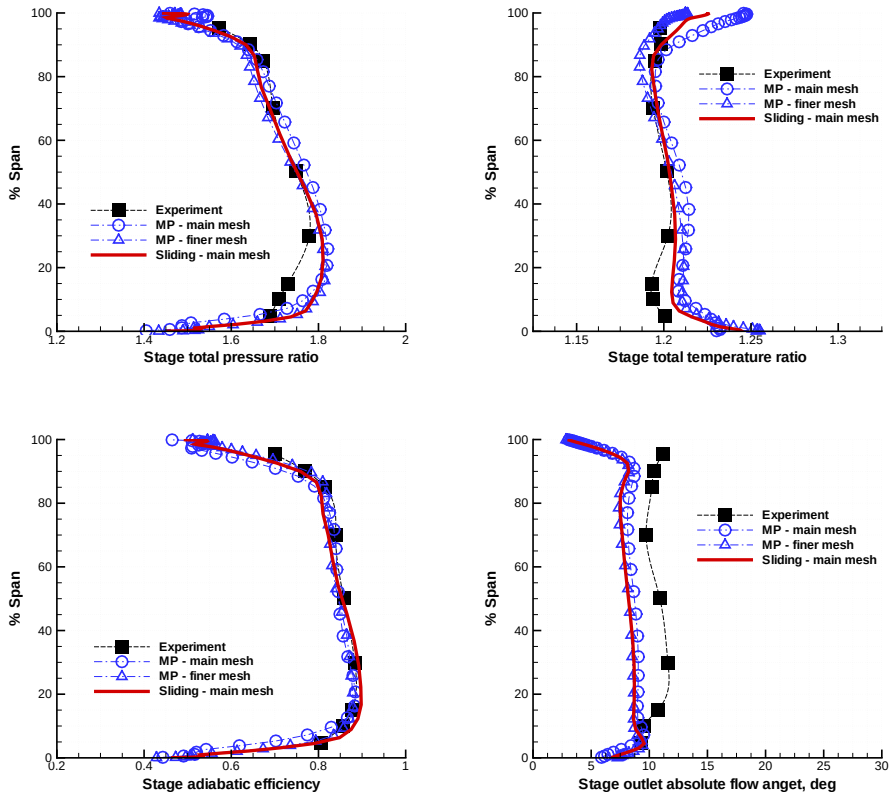

Figure 5: Predicted pitch averaged radial profiles at 4004 including stage total pressure ratio, total temperature ratio, adiabatic efficiency and outlet absolute flow angle

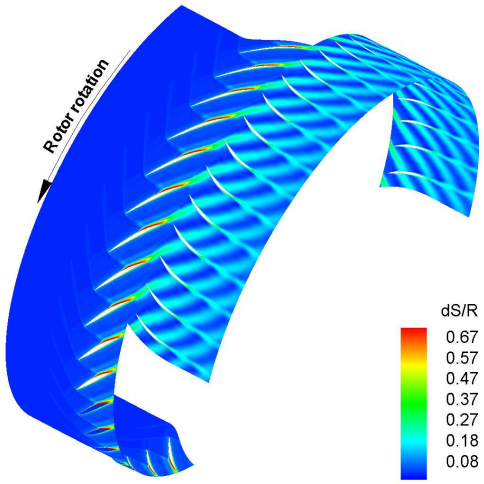

Figure 6: Instantaneous entropy contour at mid span of NASA stage 35

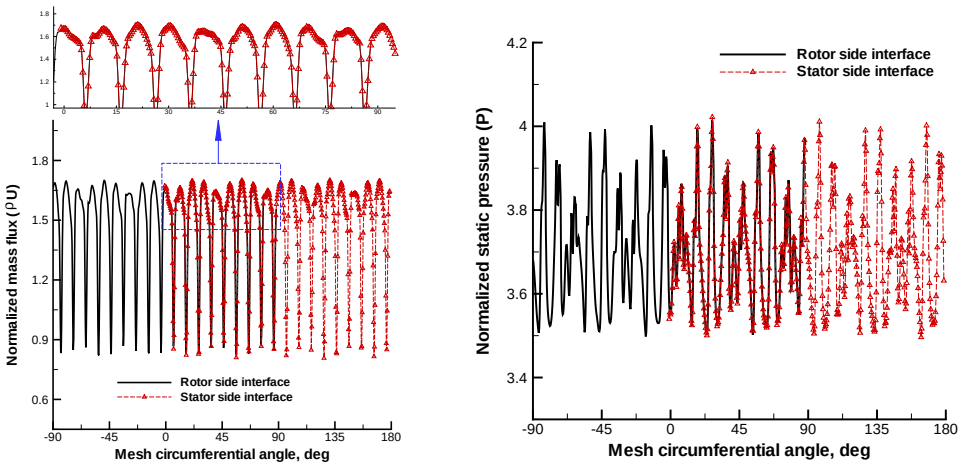

Figure 7: Instantaneous normalized mass flux ρU (top) and static pressure P (bottom) at mid span of the rotor/stator interface

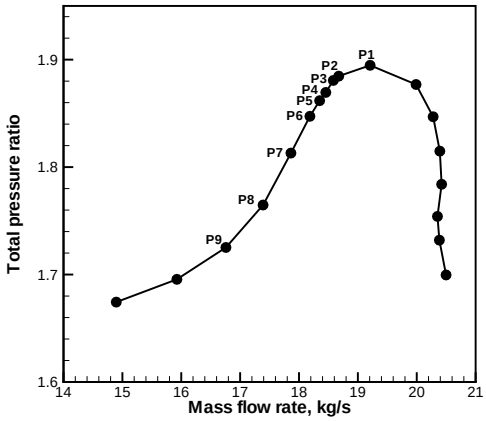

Figure 8: Predicted unsteady speedline with full annulus simulation

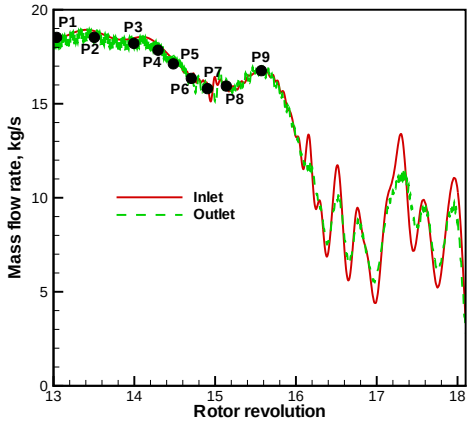

Figure 9: Mass variation during stall

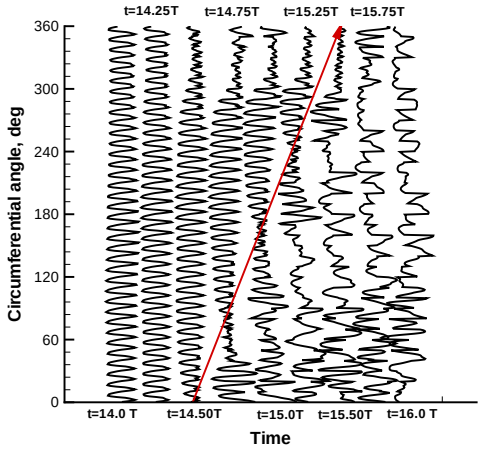

Figure 10: Time traces of circumferential pressure at tip span

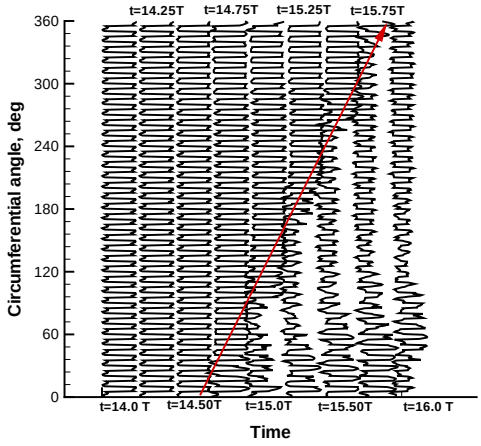

Figure 11: Time traces of circumferential axial velocity at tip span

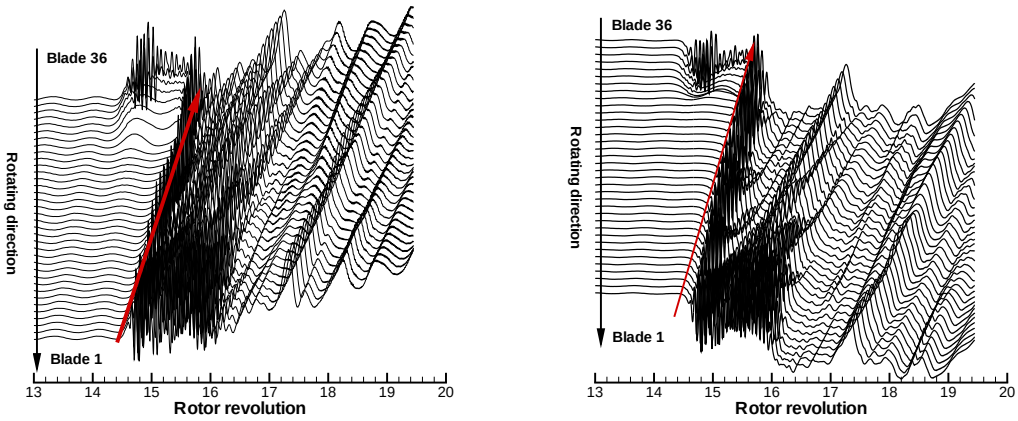

Figure 12: Variations of pressure and axial velocity at tip span

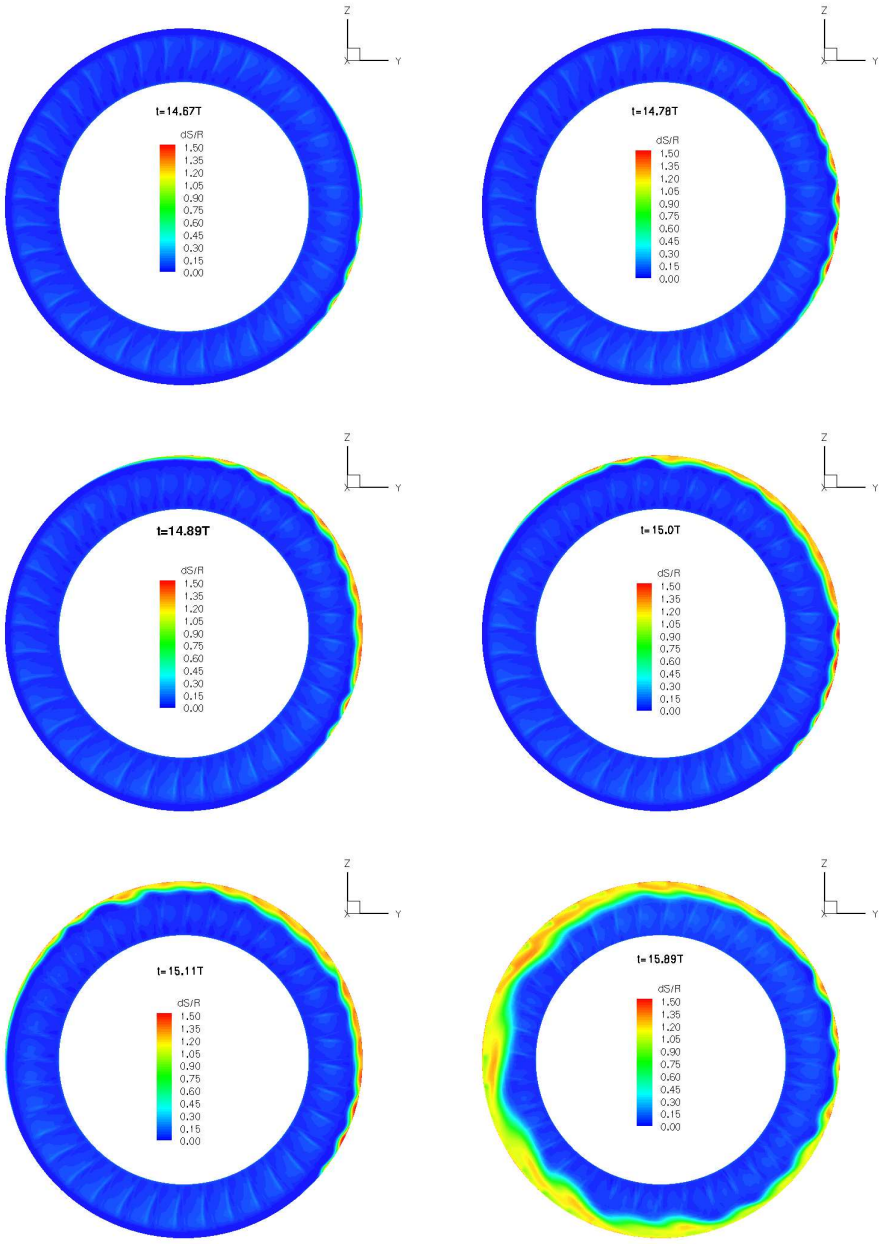

Figure 13: Entropy change of axial cross section near rotor leading edge

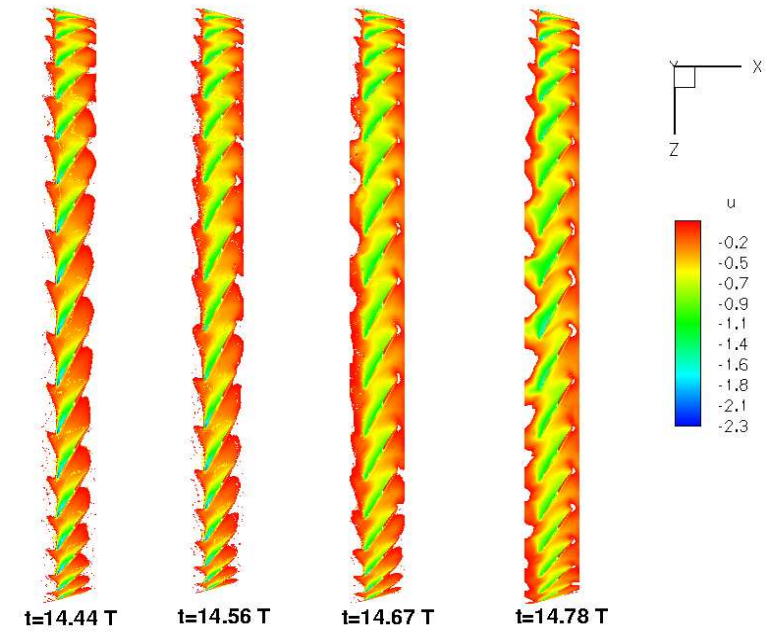

Figure 14: Contour of negative axial velocity at the rotor tip span

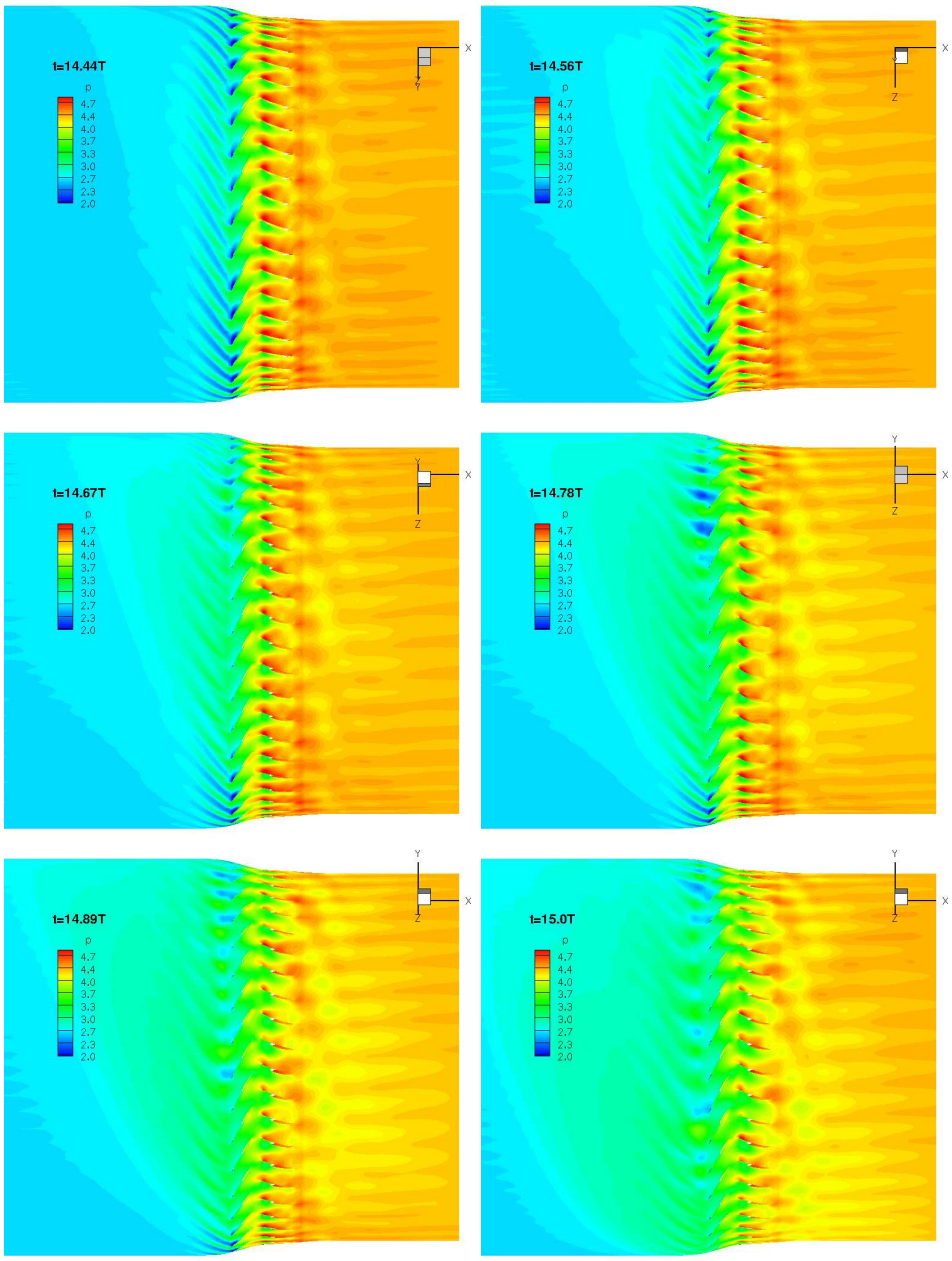

Figure 15: Static pressure at the tip clearance

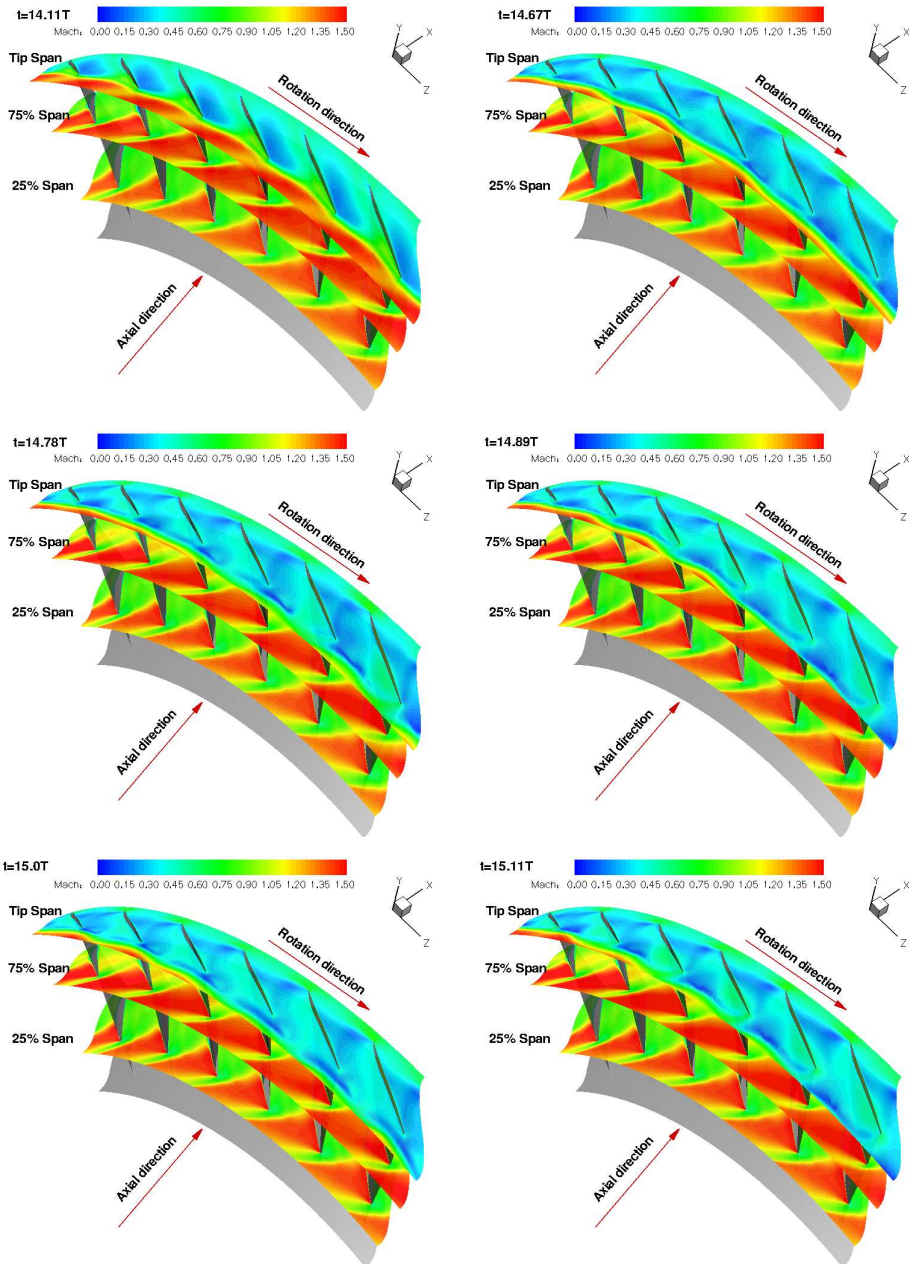

Figure 16: Mach contours across the starting stall cell

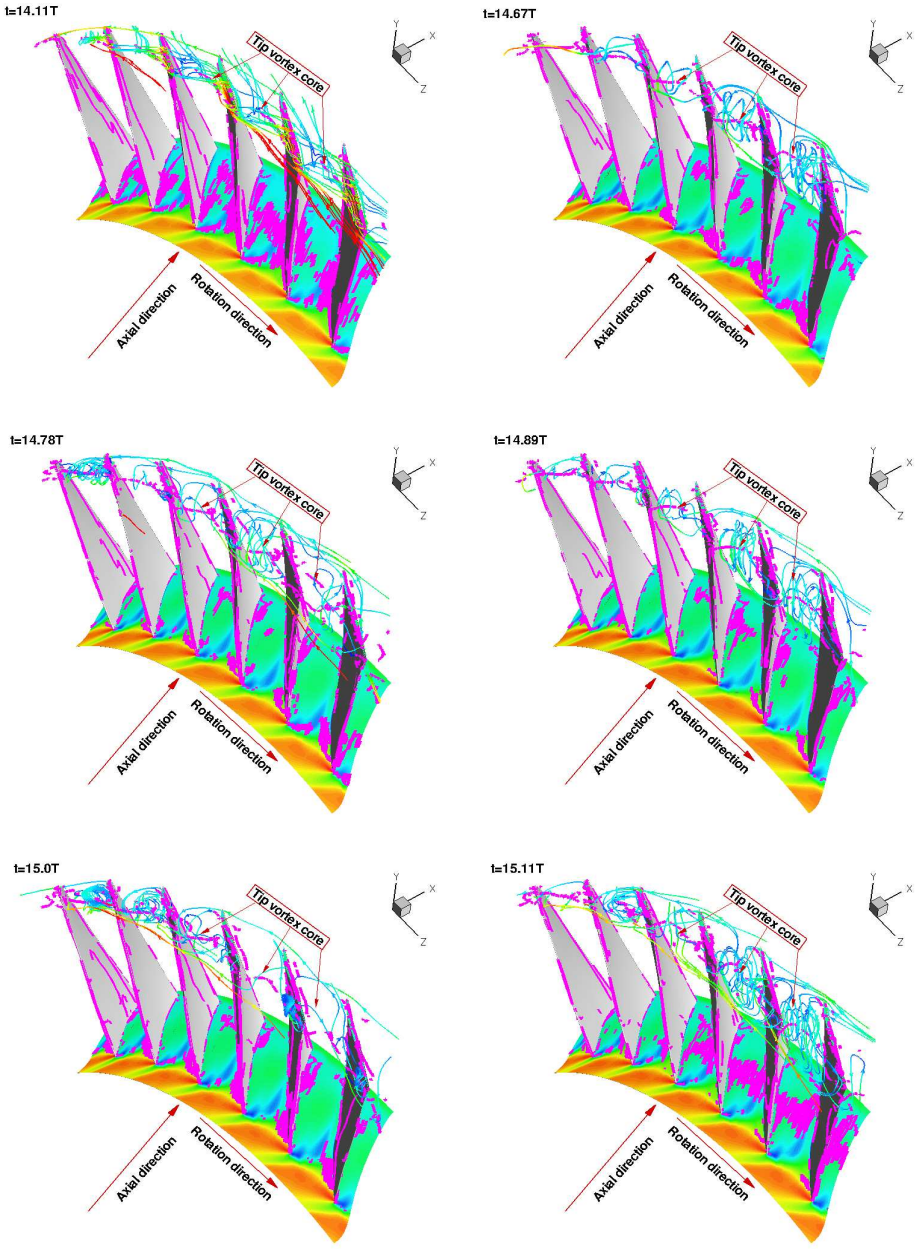

Figure 17: Tip clearance vortex trajectory at different instances

References

[1] K. Yamada, M. Furukawa, and K. Funazaki, "Numerical Analysis of Tip Leakage Flow Field in a Transonic Axial Compressor Rotor." IGTC2003 Tokyo TS-030, Proceedings of the International Gas Turbine Congress 2003, 2003.

[2] C. Hah, D.C. Rabe, and A.R. Wadia, "Role of Tip-Leakage Vortices and Passage Shock in Stall Inception in a Swept Transonic Compressor Rotor." GT2004-53867, Proceedings of ASME Turbo Expo 2004, 2004.

[3] N. Reuss, and C. Mundt, "Experimental Investigations of Pressure Distortions on the High-Pressure Compressor Operating Behavior," *Journal of Propulsion and Power*, vol. 25, pp. 653–667, doi: 10.2514/1.37412, 2009.

[4] M. Zake, L. Sankar, and S. Menon, "Hybrid Reynolds-Averaged Navier-Stokes/Kinetic-Eddy Simulation of Stall Inception in Axial Compressors," *Journal of Propulsion and Power*, vol. 26, pp. 1276–1282, doi: 10.2514/1.50195, 2010.

[5] R. Davis, and J. Yao, "Computational Approach for Predicting Stall Inception in Multistage Axial Compressor," *Journal of Propulsion and Power*, vol. 23, pp. 257–265, doi: 10.2514/1.50195, 2007, doi: 10.2514/1.18442.

[6] D.A. Hoying, C.S. Tan, H.D. Vo, and E.M. Greitzer, "Role of Blade Passage Flow Structures in Axial Compressor Rotating Stall Inception," *AMSE J. of Turbomach.*, vol. 121, pp. 735–742, doi:10.1115/1.2836727, 1999.

[7] H.D. Vo, C.S. Tan, and E.M. Greitzer, "Criteria for Spike Initiated Rotating Stall," *AMSE J. of Turbomach.*, vol. 130, pp. 1–8, doi:10.1115/1.2750674, 2008.

[8] J. Chen, B. Johnson, M. Hathaway, and R. Webster, "Flow Characteristics of Tip Injection on Compressor Rotating Spike via Time-Accurate Simulation," *Journal of Propulsion and Power*, vol. 25, pp. 678–687, doi: 10.2514/1.41428, 2009.

[9] J. Chen, M. Hathaway, and G. Herrick, "Prestall Behavior of a Transonic Axial Compressor Stage via Time-Accurate Numerical Simulation," *AMSE J. of Turbomach.*, vol. 130, pp. 1–12, doi:10.1115/1.2812968, 2008.

[10] H.S. Im, X.Y. Chen, and G.C. Zha, "Detached Eddy Simulation of Stall Inception for a Full Annulus Transonic Rotor," *Journal of Propulsion and Power*, vol. 28 (No. 4), pp. 782–798, doi: 10.2514/1.58970, 2012.

[11] P.R. Spalart, W.H. Jou, M. Strelets, and S.R. Allmaras, "Comments on the Feasibility of LES for Wings, and on a Hybrid RANS/LES Approach." Advances in DNS/LES, 1st AFOSR Int. Conf. on DNS/LES, Greyden Press, Columbus, H., Aug. 4-8, 1997.

[12] G.C. Zha, Y.Q. Shen, and B.Y. Wang, "An Improved Low Diffusion E-CUSP Upwind Scheme ," *Journal of Computer and Fluids*, vol. 48, pp. 214–220, 2011, doi:10.1016/j.compfluid.2011.03.012.

[13] Y.Q. Shen, G.C. Zha, and B.Y. Wang, "Improvement of Stability and Accuracy of Implicit WENO Scheme," *AIAA Journal*, vol. 47, pp. 331–334, DOI:10.2514/1.37697, 2009.

[14] Y.Q. Shen, B.Y. Wang, and G.C. Zha, "Implicit WENO Scheme and High Order Viscous Formulas for Compressible Flows ." AIAA Paper 2007-4431, 2007.

[15] B. Wang, Z. Hu, and G. Zha, "A General Sub-Domain Boundary Mapping Procedure For Structured Grid CFD Parallel Computation," *AIAA Journal of Aerospace Computing, Information, and Communication*, vol. 5, pp. 425–447, 2008.

[16] P.R. Spalart, and S.R. Allmaras, "A One-equation Turbulence Model for Aerodynamic Flows." AIAA-92-0439, 1992.

[17] A. Jameson, "Time Dependent Calculations Using Multigrid with Applications to Unsteady Flows Past Airfoils and Wings." AIAA Paper 91-1596, 1991.

[18] H.S. Im, X.Y. Chen, and G.C. Zha, "Simulation of 3D Multistage Axial Compressor Using a Fully Conservative Sliding Boundary Condition." ASME IMECE2011-62049, International Mechanical Engineering Congress & Exposition, Denver, November 2011, 2011.

[19] L. Reid, and R.D. Moore, "Design and Overall Performance of Four Highly-Loaded, High Speed Inlet Stages for an Advanced, High Pressure Ratio Core Compressor." NASA TP.1337, 1978.

[20] Adamczyk, J. J., Celestina, M. L., and Greitzer, E. M., "The Role of Tip Clearance in High-Speed Fan Stall," *Journal of Turbomachinery*, vol. 115, pp. 22–38, 1993.

[21] W. W. Copenhaver, E. R. Mayhew, E. R., C. Hah, and A. R. Wadia, "The Effects of Tip Clearance on a Swept Transonic Compressor Rotor," *Journal of Turbomachinery*, vol. 118, pp. 230–239, 1996.

[22] D. E. Van Zante, A. J. Strazisar, J. R. Wood, M. D. Hathaway, T. H. Okiishi, "Recommendations for Achieving Accurate Numerical Simulation of the Tip Clearance Flows in a Transonic Compressor Rotor," *Journal of Turbomachinery*, vol. 122, pp. 733–742, 2000.

[23] D. C. Rabe, C. Hah, "Application of Casing Circumferential Grooves for Improved Stall Margin in a Transonic Axial Compressor." ASME Paper GT-2002-30641, 2002.